One-degree-of-freedom galloping instability of a 3D bluff body pendulum at high Reynolds number

Antoine Myskiw, Yann Haffner, François Paillé, Jacques Borée, Christophe Sicot

One-degree-of-freedom galloping instability of a 3D bluff body pendulum at high Reynolds number

Antoine Myskiw [(1)], Yann Haffner [(2)], François Paillé [(1)], Jacques Borée [(1)] and Christophe Sicot [(1)]

[(1)] *Institut Pprime - UPR 3346, CNRS-ENSMA-Université de Poitiers, 86360 Futuroscope-Chasseneuil, France*

[(2)] *Centre Scientifique et Technique du Bâtiment (CSTB), 44323 Nantes, France*

Abstract

The cross-flow swinging dynamics of a cube pendulum is studied experimentally in a flow at high Reynolds numbers ($Re \sim 10^5$) with a low free-stream turbulence intensity. A galloping instability is observed and results in the exponential growth of the swinging motion. The onset of galloping is found to be very sensitive to the static yaw angle of the cube. Despite the 3D geometry of the cube, flow mechanisms similar to the case of a square cylinder appear to govern the onset of the instability. A quasi-steady linear model of the motion is assessed to predict the stability of the pendulum.

For the lowest reduced velocity investigated ($U^* = 18.5$), unsteady phenomena arise during the saturation phase of the pendulum oscillations. From the analysis of the unsteady loads and the pressure distribution on the faces of the cube, an unsteady phase delay between the wake and the pendulum dynamics is identified. It produces an energy loss in the pendulum motion which favors its saturation.

Keywords – galloping instability, pendulum, 3D bluff body, unsteady

1 Introduction

Fluid-structure interactions (FSI) involving bluff bodies is a wide subject raising issues ranging from structural safety in wind or water engineering to energy harvesting from flows [1]. FSI on bidimensional cylindrical bodies have been extensively studied [2, 3, 4, 5, 6] (non exhaustive list) and have multiple practical applications in civil and aeronautical engineering, for instance in the design of slender buildings, bridge decks

or aircraft wings. Less investigated, FSI between a tridimensional tethered bluff body and the surrounding wind has nevertheless an importance in many cases, such as loads lifted by a helicopter [7] or a tower crane [8, 9]. In these cases, control laws based on models of the pendulum dynamics can be used to reduce the oscillations and stabilize the system [7, 9]. Cable car engineering is an application closer to this study, where FSI raises several issues concerning the safety, comfort, and availability of the lines. A few studies tackle the sensitivity of a cable car to the wind and the safety engineering still relies on basic criteria and requires periodic checks [10]. The existing works on the subject mainly focus on field measurements, on modelling of the pendulum dynamics [11] and on the vertical oscillations induced by the cables [12], but the aerodynamic mechanisms responsible for the pendulum oscillations are not characterized.

The type of FSI that may occur is related to the reduced velocity U^*. It is defined as the ratio between the advective frequency of the flow U_0/D - based on the free stream velocity U_0 and the side length D of the solid - and the natural frequency f_0 of the solid [13, 6]. Two main distinct mechanisms of interaction leading to FSI may arise between a bluff body and the surrounding flow: modal coupling such as vortex-induced vibration (VIV) and aerodynamic coupling such as flutter, including galloping. On a bidimensional square cylinder, VIV tend to occur at a reduced velocity around 7-8 [14, 15, 13], whereas galloping occurs over a wide range of reduced velocities limited by a lower critical velocity driven by mass and damping parameters of the system [2, 16]. Galloping is a common phenomenon. A typical example in wind engineering is the galloping instability of the deck of a bridge that appears as a cross-flow oscillation or/and a torsional motion [17]. The shape of the bluff body is the main parameter governing the apparition of a galloping instability because of the sensitivity of the mean aerodynamic loads to the attitude of the body. The galloping instability of bidimensional cylinders has been extensively studied, in particular on the rectangular cylinder [18, 19, 15] (non-exhaustive list). However, the problem of a tridimensional bluff body in FSI is less commonly tackled due to its increased flow complexity [20, 21, 22], and most of the existing studies focus on low Reynolds numbers and VIV.

Nakamura [15] offers an understanding of the basic mechanism of the galloping instability occurring on a rectangular cylinder from flow visualizations and local pressure measurements. On both sides of the static prism, the flow separates at the leading edges and does not reattach as the aspect ratio - defined as the length over the cross-stream thickness of the section - is low enough, creating a large recirculation region with the wake with nearly constant pressure distribution along both lateral sides. A high reduced velocity ensures that a transversal motion of the body is slow enough not to produce an pitch angle that could cause flow reattachment on the windward side. Thus, during a transversal motion, the shear layer on the motion side (windward side) moves closer to the body and becomes more curved, whereas the shear layer on the leeward side moves away from it and becomes less curved. Consequently, the pressure on both sides is unbalanced with a stronger depression on the windward side, resulting in a global aerodynamic force that amplifies the motion. For bidimensional rectangular cylinders, the aspect ratio of the cross-section is an important parameter driving the onset of transverse galloping [2, 18]. In a flow with low free-stream turbulence intensity, galloping is observed for an aspect ratio lower than 2 [23]. An aspect ratio of 3 or larger allows the flow to reattach on the sides, which tends to stabilize the system [18]. The upstream flow turbulence also influences the stability as it influences the flow reattachment on the sides [4, 23].

To the best of the authors' knowledge, no study in the literature investigates the mechanisms of transverse galloping occurring on tridimensional parallelepipeds in

comparison with bidimensional rectangular cylinders.

The paper tackles the the swinging motion induced by galloping observed on a tethered tridimensional bluff body - a cube pendulum - at high Reynolds numbers ($Re \sim 10^5$) and high reduced velocities. It is organized as follows. The experiments are described in section 2. A quasi-steady approach is assessed to characterize the stability of the cube pendulum in section 3. An analysis of the pressure distribution over the static cube at various yaw angles is provided in section 4. Finally, the swinging motion of the cube pendulum is investigated in section 5.

2 Experiments and measurement methods

2.1 Main characteristics of the setups

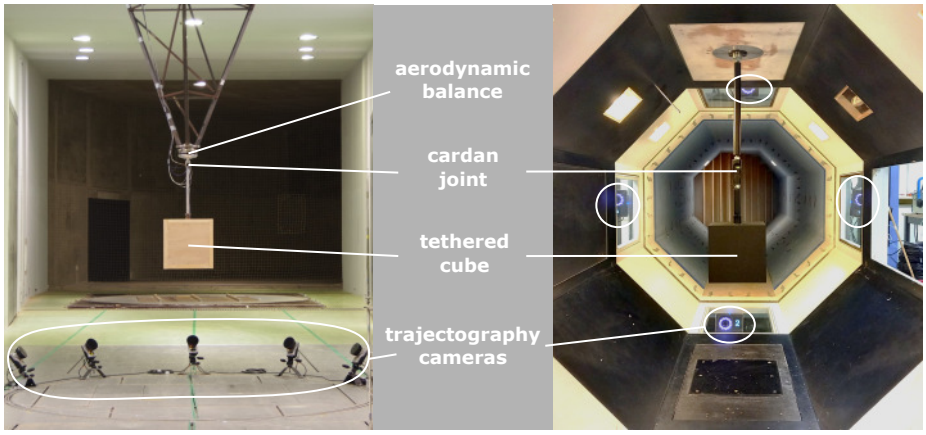

Figure 1: Pictures of the two setups: the Jules Verne setup on the left and the S120 setup on the right

Two complementary setups involving a tethered cube in two subsonic closed-loop wind tunnels at two different scales are used. An experiment is performed inside the S120 wind tunnel at ISAE-ENSMA and another one inside the Jules Verne (JV) wind tunnel of CSTB in Nantes. In both experiments, a cube is connected by a rod to a cardan joint attached to a rigid steel structure (figure 1). The tethered cube in the JV setup is 2.5 times larger than the one in the S120 setup. The cardan joints are made of two almost perfect bearings and one bearing is blocked to allow only one degree of freedom (DoF): the circular motion around the free stream direction as illustrated in figure 2a. The mechanical damping of each bearing has been experimentally characterized and is one to two orders of magnitude smaller than the aerodynamic damping for both experiments. Table 1 introduces the main characteristics of the two setups.

Setup	$A\ (m^2)$	$D\ (m)$	$H\ (m)$	$m\ (kg)$	$\lambda_m\ (\ s^{-1})$
S120	1.2	0.2	0.2	3.3	5×10^{-3}
JV	30	0.5	0.6	19.8	1.5×10^{-3}

Table 1: Main characteristics of the setups: the area A of the test section, the side length D of the cube, the length H of the rod, the mass m of the tethered system, and the mechanical damping λ_m of the bearing

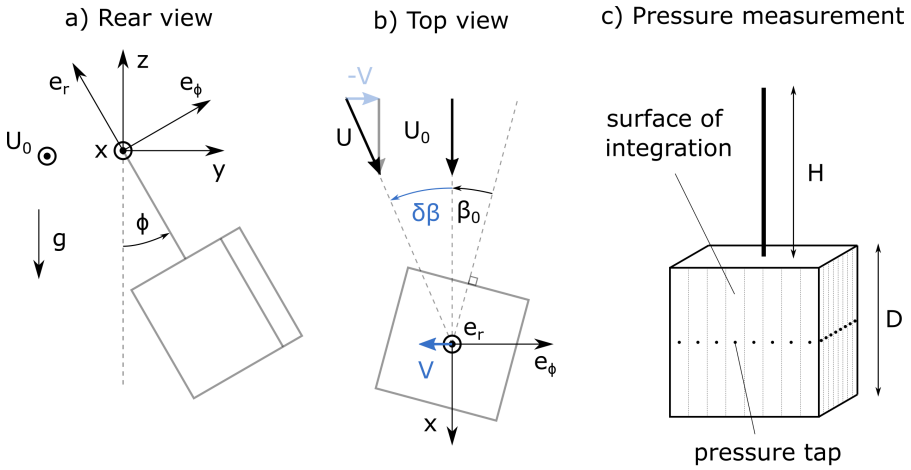

Figure 2: (a, b) Conventions used in the study: pendulum angle relative to the vertical axis ϕ, static yaw angle β_0 and dynamic yaw angle $\delta\beta$ of the cube (c) Position of the pressure probes and integration surfaces on the cube for the derivation of the aerodynamic loads

Ramamurthy and Lee [24] showed that the influence of the wall proximity on the drag coefficient of a prism with an equilateral triangle section can be neglected when the distance of the prism to the wall is larger than the characteristic length of the prism section. For a circular cylinder, this distance increases up to twice the cylinder diameter. Even if a tethered cube is not a prism, this information leads us not to consider the measurements when the cube makes an angle larger than 15° with the vertical axis in the S120 setup, which corresponds to a maximal distance of $2D$ between the edges of the body and the walls of the test section. On the opposite, the influence of the walls can be neglected in the JV setup for all angles of oscillation as the minimal distance between the walls and the swinging cube is 4 times larger than the side length of the cube D.

The blockage ratio in the S120 and the JV setups is 3.4% and 0.8% respectively. It remains below 5% so it is expected to have a negligible impact on the measured aerodynamic coefficients and no correction was applied on the measured coefficients [25, 26, 27]. In both wind tunnels the free-stream turbulence intensity is below 1%.

2.2 Two complementary setups

The reduced velocity U^* is defined as :

$$U^* = \frac{U_0}{D\, f_0} \tag{1}$$

It is an important parameter of this study that represents the ratio between the period of the swinging motion $T_0 = 1/f_0$ – here expressed from the natural frequency of the swinging motion f_0 – and the advective time-scale of the flow D/U_0. The pendulum frequency f_0 is expressed from the distance L between the center of gravity of the system to the fixed point. In both setups, the rod is light enough compared to the cube so that the center of gravity of the whole system can be approximated as the barycentre of the cube: $f_0 = \sqrt{g/L}$ and $L = H + D/2$. Thus, according to eq. 1, the larger the scale of the cube pendulum, the lower U^*.

Despite their similarity, the two setups are used in different and complementary ways. Two different scales are studied to investigate a wide range of reduced velocities. The S120 setup focuses on a single high reduced velocity, whereas a wide range of lower reduced velocities is investigated in the JV setup. The lowest U^* investigated is below the critical value of $U^* = 20$ given by Blevins [13] above which no unsteady phenomena is expected to occur.

The S120 setup is used to study the sensitivity of the stability of the system to the static yaw angle β_0 of the cube at a constant free stream velocity U_0, so at a constant U^*. This angle, illustrated in figure 2b, corresponds to the angular position of the cube around the rod that can be set before any experiment: the cube cannot rotate around the rod during the motion. In this setup, the experimental system dynamics are confronted with a quasi-steady model built to predict the stability of the pendulum.

In the JV setup, the angle β_0 is blocked at $0°$, so the free stream is normal to the front face of the cube. The uncertainty on β_0 is $\pm 1°$ and can lead to slight asymmetries in the dynamics of the pendulum oscillation. However, this uncertainty remains small enough to be expected to not influence the aerodynamic mechanisms driving the motion. In this configuration, galloping instability occurs and is investigated with pressure measurements at different flow speeds, so at different reduced velocities.

Table 2 summarizes the ranges of the parameters investigated in each setup.

Setup	β_0 (°)	U_0 (m/s)	U^*	Re
S120	$[0, 45]$	15	82.4	1.9×10^5
JV	0	$[4.8, 14.6]$	$[18.5, 57]$	$[1.5, 4.7] \times 10^5$

Table 2: Parameters investigated in the two setups: static yaw angle β_0, mean flow velocity U_0, reduced velocity U^* and Reynolds number Re

2.3 Metrology

In both setups, motion tracking by cameras is performed on the cube. The cameras are visible in figure 1. In the S120 setup, 4 Vicon V5 5Mpx cameras with a focal length of 12.5mm track 4 circular markers of diameter $0.01D$ on the rear face of the cube at a rate of 200Hz. In the JV setup, 5 Qualisys Oqus 4Mpx cameras with a focal length of 20mm track 4 circular markers of diameter $0.02D$ on the bottom face of the cube at a rate of 200Hz. In addition to the motion tracking system in the JV setup,

a set of 2 unidirectional accelerometers Kistler 8316A with a range of $\pm 10g$ is used. These are sensitive to both static and dynamic movements and provide the angles of the pendulum to the vertical axis with $\pm 0.5^\circ$ of uncertainty.

In the S120 setup, a strain gauge 6-component aerodynamic balance is used to provide the static aerodynamic loads on the cube with a maximal uncertainty of $\pm 5\%$ at the reference speed $U_0 = 15m/s$. The balance is mounted inside a profiled arm lifting the cube from the ground of the wind tunnel. In the JV setup, the static loads on the tethered cube are measured using an ATI Omega 170 strain gauge 6-component aerodynamic balance, mounted at the base of the steel structure over the cardan joint (figure 1), with an uncertainty of $\pm 3\%$ on the measured loads for the reference configuration at $U_0 = 15m/s$. In both setups, the average aerodynamic loads on the cube over at least 2 minutes are measured with the balance at static yaw angles between 0° and 45°. This range can then be extended to $[-180^\circ, 180^\circ]$ by symmetry considerations.

The whole arrangement of the JV setup including the tethered cube and the steel structure has been dynamically characterized in both torsion and flexion to ensure that its structural behavior would not interfere with the measurements or in the fluid-structure coupling. The main modes of the structure appear decoupled from the pendulum dynamics.

Local unsteady pressure measurements are performed with a corona of 32 pressure taps on the front, rear, and lateral faces of the JV cube as depicted in figure 2c. These pressure taps are linked by 1m long vinyl tubings to two pressure scanners PSI 32HD of $\pm 2500Pa$ range. The measurements are a posteriori corrected to compensate for the pressure distortions induced by the tubings using a priori calibration of the tubing system on an in-house test bench. The frequency response of the system is flat on the whole range of measurement up to the sampling frequency of 200Hz. This frequency is 2 orders of magnitude larger than the pendulum frequency ($\sim 0.5Hz$) and much larger than the advective frequency of the flow ($U_0/D \leq 30Hz$). For the reference configuration in a mean flow at $U_0 = 15m/s$, measurements have an uncertainty of $\pm 5\%$ of the reference dynamic pressure. Reference conditions (static pressure, temperature, and air humidity) are taken in the test section at a distance 5D upstream of the location of the pendulum to ensure homogeneous flow conditions.

Finally, local pressures are used to compute the aerodynamic loads by integration over the cube faces. On the lateral, rear, and front faces, each local pressure is associated with a vertical strip depicted in figure 2c, and added up to compute the global pressure loads acting on the face. The aerodynamic loads are then derived from the pressure loads measured on each face. This approximation of the aerodynamic loads is based on a corona of pressure probes because the 3D distribution of static wall pressure is not available in this experiment. However, the resulting mean static loads match well with the static loads measured with the aerodynamic balance (figure 3), with a maximal difference of 4.5% relative to the mean drag coefficient measured with the balance. This observation for the 3D cubic geometry is very important because this methodology provides a straightforward way to determine experimentally the dynamic loads on the swinging cubes and to discuss the departure from quasi-steady flow conditions. The static aerodynamic coefficient $C_\phi = C_L cos(\beta_0) + C_D sin(\beta_0)$ is the component of the aerodynamic force normal to the lateral faces of the cube, with C_D and C_L the drag and lift coefficients respectively. C_D is in the streamwise direction and C_L is orthogonal to the free-stream and to the pendulum arm axis. This axis corresponds to the direction of motion when the cube is oscillating with no initial yaw angle β_0, which is the main focus of this study.

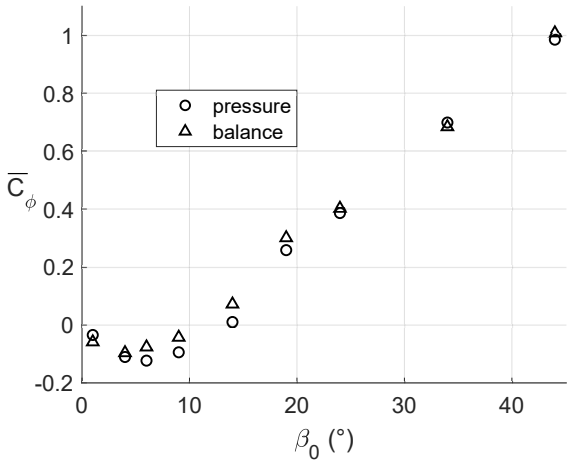

Figure 3: Comparison between the static mean aerodynamic coefficient C_ϕ derived from the pressure measurements and the one measured with the balance in the JV setup, according to the static yaw angle β_0

3 Stability analysis

3.1 Quasi-steady model of the bluff body pendulum dynamics

The stability of the pendulum system is assessed using the quasi-steady theory that allows to use of the mean static aerodynamic loads measured on the tethered bluff body in the pendulum momentum equation around equilibrium. The linearization of this equation for a small angular displacement from equilibrium reduces the pendulum dynamics to a second-order differential equation whose damping term drives the stability of the system. All the steps are described below.

To simplify the problem, the weight and the aerodynamic force are applied at the center of mass of the cube, which is supposed aligned with the rod at a distance L from a perfect pivot joint. The aerodynamic effect of the rod on the motion is neglected compared to that of the cube. In the following equations, $g = 9.81 m/s^{-2}$ is the gravitational acceleration, ρ the air density, $S = D^2$ the reference surface of the cube, $\overrightarrow{U_0}$ the mean flow velocity, $\overrightarrow{U}$ the apparent flow velocity and $\overrightarrow{V}$ the cube velocity (figure 2b). The axis system is chosen such that the freestream velocity U_0 is aligned with the $\vec{x}$ axis. The cylindrical coordinate system $(\vec{e_r}, \vec{x}, \vec{e_\phi})$ is used to put in equations the cross-flow swinging motion of the cube as sketched in figure 2. The origin is located at the fixed pivot joint, which is the center of rotation of the system. ϕ is the angle made by the pendulum with the vertical axis. The mean angle $\bar{\phi}$ for which the static momentum balance is achieved between the aerodynamic loads on the cube pendulum and its weight depends on the static yaw angle of the cube β_0. C_D and C_L represent the drag and lift coefficients of the tethered cube and C_ϕ represents the aerodynamic coefficient along the axis of motion $\vec{e_\phi}$: $C_\phi(\beta, t) = C_D(\beta, t)sin(\delta\beta) + C_L(\beta, t)cos(\delta\beta)$. These coefficients correspond to the aerodynamic loads scaled by $0.5\rho S U^2$. An upper bar is used to write the mean static aerodynamic coefficients. The momentum equation

at equilibrium projected along $\vec{e_\phi}$ reads:

$$-mg\ sin(\bar{\phi}(\beta_0)) + \frac{1}{2}\rho S U_0^2\ \overline{C_\phi}(\beta_0) = 0 \tag{2}$$

When the tethered cube is oscillating with a velocity $\vec{V} = L\dot{\phi}\ \vec{e_\phi}$, the squared magnitude of the apparent velocity is $U^2 = U_0^2 + V^2$ and the effective yaw angle of the oncoming freestream is $\beta = \beta_0 + \delta\beta$ where $\delta\beta = -arctan(V/U_0)$ represents the dynamic yaw angle depicted in figure 2b. The momentum balance for the system projected along $\vec{e_\phi}$ reads:

$$mL\ \ddot{\phi} = -mg\ sin(\phi) + \frac{1}{2}\rho S U^2\ C_\phi(\beta, t) \tag{3}$$

Then, subtracting the static balance (eq. 2) from the momentum balance (eq. 3) gives the momentum equation around equilibrium (eq. 4):

$$mL\ \ddot{\phi} = -mg\ \left[sin(\phi) - sin(\bar{\phi}(\beta_0))\right] + \frac{1}{2}\rho S\left[U^2\ C_\phi(\beta, t) - U_0^2\ \overline{C_\phi}(\beta_0)\right] \tag{4}$$

At this point, two hypotheses are introduced. First, the quasi-steady hypothesis, which supposes U^* high, allows to consider aerodynamic coefficients as slowly varying in time and thus to approximate them as the mean static aerodynamic coefficients: $C_i(\beta, t) = \overline{C_i}(\beta)$ for C_D, C_L and C_ϕ. The validity of the quasi-steady hypothesis will be discussed in this paper. Secondly, small angular displacements from the equilibrium position $\varepsilon = \phi - \bar{\phi}$ are considered so that equation 4 can be linearized at first order in ε. This approximation is justified because the linear model focuses on the onset of the instability, so for small displacements around the equilibrium. This supposes $\delta\beta = -L\dot{\varepsilon}/U_0$ at first order in $\dot{\varepsilon}$ and allows to linearize the aerodynamic term of equation 4 in $\delta\beta$.

$$\overline{C_\phi}(\beta) = \overline{C_\phi}(\beta_0) + \delta\beta\ \left.\frac{d\overline{C_\phi}}{d\beta}\right|_{\beta_0} + o(\delta\beta) \tag{5}$$

$$\left.\frac{d\overline{C_\phi}}{d\beta}\right|_{\beta_0} = \overline{C_D}(\beta_0) + \left.\frac{d\overline{C_L}}{d\beta}\right|_{\beta_0} + o(1) \tag{6}$$

$$sin(\phi) - sin(\bar{\phi}(\beta_0)) = cos(\bar{\phi}(\beta_0))\ \varepsilon + o(\varepsilon) \tag{7}$$

Finally, the linearization of equation 4 using the linearized expressions (eqs. 5, 6, 7) gives a second order differential equation in ε (eq. 8) with the pseudo-frequency ω_0 (eq. 9) and the aerodynamic damping coefficient λ (eq. 10) of the linear model. λ' (eq. 11) represents the reduced aerodynamic damping coefficient depending only on the mean static aerodynamic characteristics of the studied bluff body. If the pendulum is vertical at equilibrium ($\bar{\phi}(\beta_0) = 0$), ω_0 is the pseudo-frequency of a free simple pendulum $\sqrt{g/L}$.

$$\ddot{\varepsilon} + 2\lambda\ \dot{\varepsilon} + \omega_0^2\ \varepsilon = 0 \tag{8}$$

$$\omega_0 = \sqrt{\frac{g}{L} cos(\bar{\phi}(\beta_0))} \tag{9}$$

$$\lambda = \frac{\rho S U_0}{4m}\ \lambda' \tag{10}$$

$$\lambda' = \left.\frac{d\overline{C_\phi}}{d\beta}\right|_{\beta_0} = \overline{C_D}(\beta_0) + \left.\frac{d\overline{C_L}}{d\beta}\right|_{\beta_0} \tag{11}$$

According to this model, the pendulum system is stable if $\lambda > 0$ and unstable if $\lambda < 0$, so $\lambda' < 0$. The system is unstable at a given angle β_0 if $\overline{C_\phi}$ exhibits a negative slope around β_0, which is equivalent to $\overline{C_D}(\beta_0) + \left.\frac{d\overline{C_L}}{d\beta}\right|_{\beta_0} < 0$. This inequation

corresponds to the Den Hartog criterion, characteristic of the galloping instability [3], showing that the transverse galloping instability is characterized by a negative static lift gradient that counterbalances the stabilizing drag.

Assuming the validity of the quasi-steady hypothesis during the swinging motion, the mean static aerodynamic loads can also be used in equation 3 to build a non-linear model simulating the pendulum oscillations.

3.2 Experimental validation of the quasi-steady model

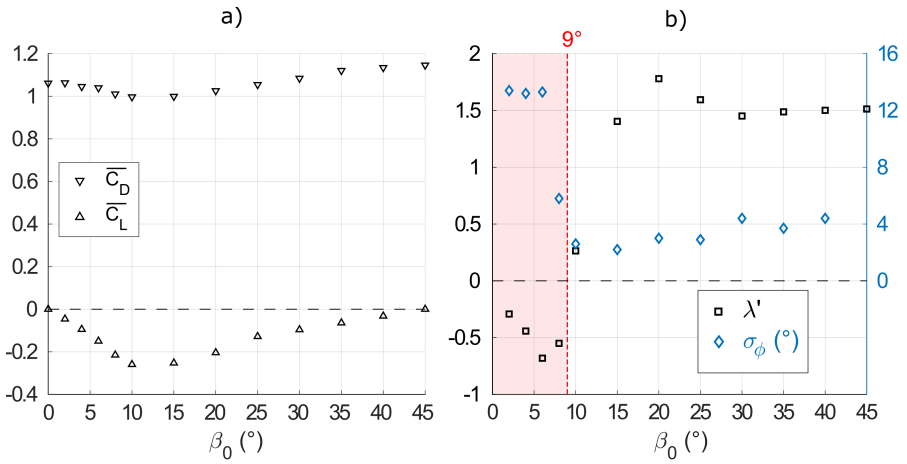

Figure 4: a) Evolution of the mean static drag and lift coefficients $\overline{C_D}$ and $\overline{C_L}$ with the static yaw angle of the cube β_0 for $U_0 = 15m/s$ for the S120 setup b) Reduced aerodynamic damping coefficient λ' of the tethered cube and standard deviation σ_ϕ of the angle ϕ derived from measurements at $U_0 = 15m/s$ for different static yaw angles β_0 for the S120 setup ; the red area shows the unstable region

The mean static aerodynamic loads on the cube are measured to draw the stability map $\lambda'(\beta_0)$ (figure 4). The drag and lift coefficients presented in figure 4a are in line with the data gathered from the literature on a square cylinder in a flow with low free-stream turbulence intensity [17, 18, 19, 28, 5]. The negative lift gradient characteristic of galloping instability is visible. From these static measurements, the quasi-steady model predicts an instability of the pendulum when $\beta_0 \in [-9°, 9°]$ (figure 4b).

Dynamic measurements are realized in the same configuration to assess the linear model for different static yaw angles β_0 from 0° to 40°. This configuration corresponds to a high reduced velocity $U^* = 82.4$ for which the quasi-steady theory is expected to be valid. An example of galloping instability occurring in the JV setup for $\beta_0 = 0$ is provided in the supplementary movie. The standard deviation of the pendulum angular position σ_ϕ in dynamic measurements is used as a qualitative indicator to visualize the range of β_0 for which galloping occurs. σ_ϕ is much higher in an unstable configuration than in a stable one, but its exact value for unstable configurations is

not relevant as the amplitude of the swinging motion grows exponentially and the experiment has to be stopped before reaching too large amplitudes. The resulting experimental unstable region is the same as the one predicted by the model (figure 4b), which validates the quasi-steady linear model as a relevant tool to predict unstable configurations of the cube pendulum.

4 Pressure distribution over the static cube

Analysis of pressure fluctuations and mean value can be used to identify and understand some key flow mechanisms in the galloping instability. The pressure distribution is measured over the cube faces in static configuration for various yaw angles $\beta_0 > 0$ in addition to the loads measured by the balance. Measurements last at least 2 minutes to get the average value $\overline{C_p}$ and the standard deviation C_p' of the pressure coefficient C_p at each probe location of the corona. The results are shown in figure 5. The front-most pressure probes on the windward and leeward sides are identified as A and B respectively. The side pressure distribution is quasi-symmetrical for low β_0 but loses its symmetry as β_0 increases, mainly due to a pressure increase at the rear part of the windward side. From $\beta_0 = 14°$, a peak of C_p' and a strong pressure increase at the rear part of the windward side is observed. This is characteristic of flow reattachment. The peak of C_p' indicates the fluctuation of the reattachment point, and the average reattachment point is expected to be located downstream this peak [29]. The location of the maximum mean pressure can be used to define a region of the windward face where instantaneous flow attachment can occur [29]. The mean location of this region is estimated as the location of the peak of C_p' and its extent as twice the distance between the maximum of $\overline{C_p}$ and the peak of C_p' and is illustrated on figure 6b. It is referred as "fluctuation zone of the reattachment point" and is obtained for several values of β_0 (figure 6a). The reattachment point moves forward as β_0 increases. The small peak of C_p' observed for $\beta_0 = 9°$ might indicate an intermittent reattachment that is not visible from mean pressure measurements. For large β_0, flow reattachment may occur very close to the upstream edge of the cube but cannot be detected with the present distribution of sensors. These patterns are similar to the ones observed in the literature on square cylinders [17, 29, 28, 5].

Before reattachment, the suction is larger on the front part of the windward side (figure 5e). This indicates non-symmetrical lateral separated regions and a higher flow velocity around the windward vertical leading edge due to the yaw angle. The shear layer on the windward side is closer to the cube and more curved after separation at the leading edge than on the leeward side [28, 30, 15]. These non-symmetric patterns produce a global aerodynamic load favorable to the galloping instability (figure 4), as observed by Nakamura on a square cylinder [15].

In figure 4a, the drag and lift curves exhibit a change of slope between $\beta_0 = 10°$ and $\beta_0 = 15°$, which is also noticed in the case of a square cylinder [17, 28]. Thus, the onset of the flow reattachment marks a drastic change of the flow pattern as $\frac{d\overline{C_\phi}}{d\beta}$ becomes positive, causing an inversion of the direction of the lateral aerodynamic load, visible through the change of sign of $\overline{C_\phi}$ around 14°.

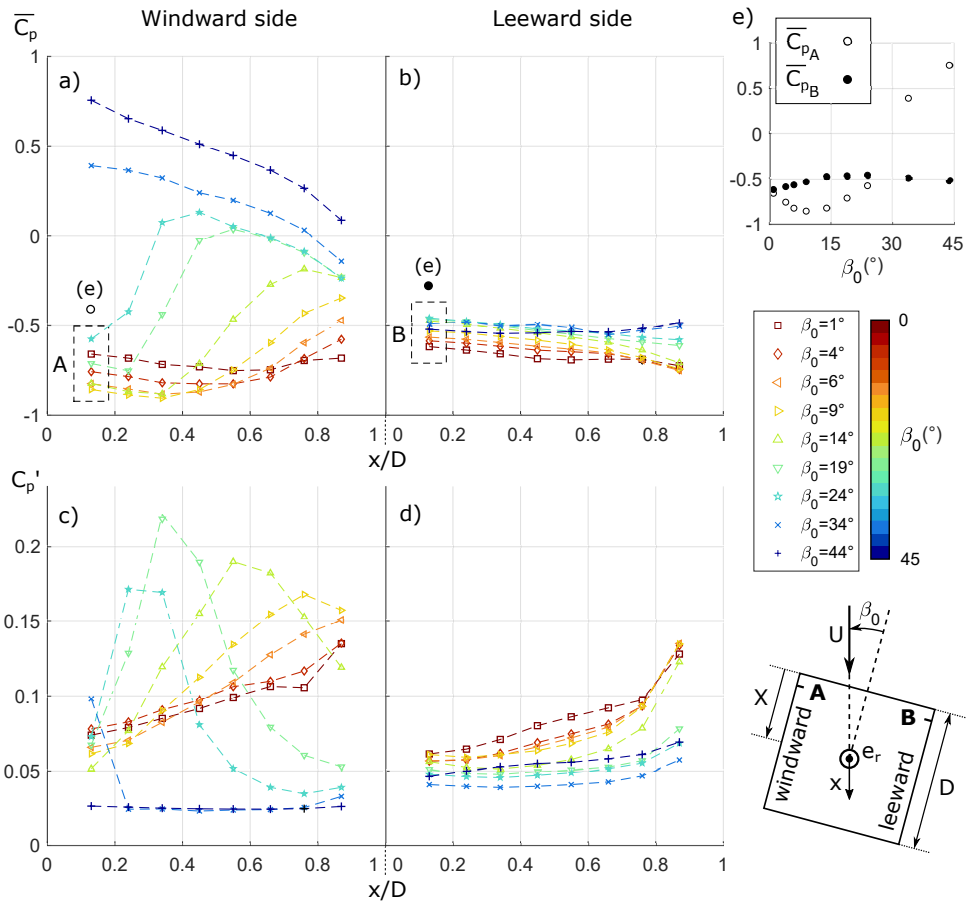

Figure 5: Distribution of $\overline{C_p}$ (a,b) and C_p' (c,d) on the lateral faces of the cube at various static yaw angles β_0 for the JV setup
e) Evolution of the $\overline{C_p}$ measured at the two frontmost probes on the windward and leeward sides, respectively $\overline{C_{pA}}$ and $\overline{C_{pB}}$, see dashed zone in a) and b) respectively

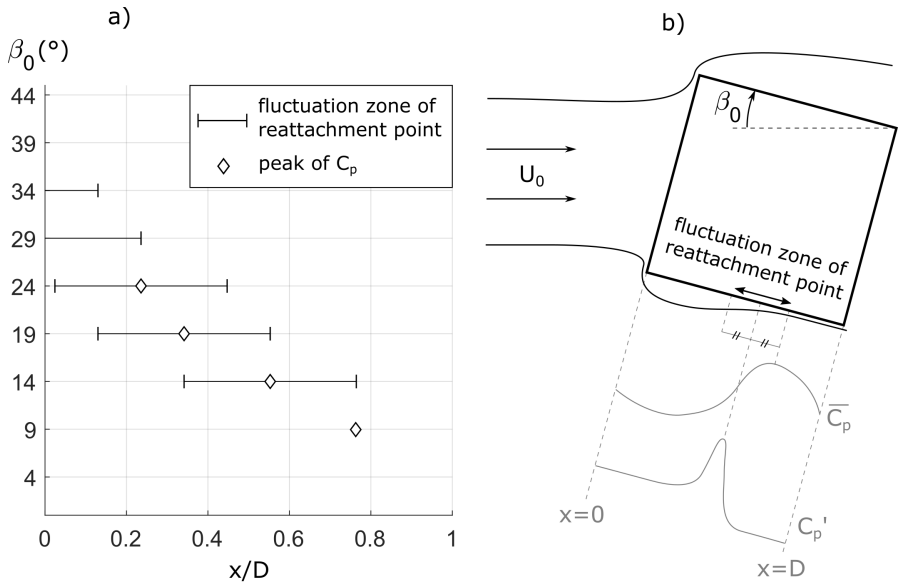

Figure 6: a) Evolution with β_0 of the fluctuation zone of the reattachment point on the windward face measured for the JV setup ; it is defined as twice the distance between the maximum of $\overline{C_p}$ and the peak of C'_p around the location of the peak of C'_p
b) 2D schematic representation of the flow reattachment with an illustration of the distribution of $\overline{C_p}$ and C'_p on the windward face

5 Swinging motion analysis

This section focuses on the experiments realized in the JV wind tunnel with the free stream normal to the front face of the cube, a configuration that exhibits galloping instability. A visualization of this instability is provided in the supplementary movie. In this specific case, $\beta_0 = 0°$ so $\beta = \delta\beta$. $|\beta|_{max}$ refers to the maximal absolute yaw angle reached in each period of oscillation. Galloping and turbulence-induced vibration cannot be properly differentiated at low amplitudes of oscillations in β. Therefore, the time origin $t = 0$ of the pendulum oscillations is set when $|\beta|_{max}$ reaches 1.5°.

5.1 Phases of the swinging motion

In all the experiments, the cube pendulum starts oscillating from rest and a quasi-exponential amplification of the amplitude of the motion is first observed. The swinging motions measured for various reduced velocities reveal a quasi-superimposed amplification of $|\beta|_{max}$ by scaling the time with the damping coefficient λ introduced in the stability analysis (eq. 10) as $t^* = -\lambda t$ (figure 7a). This similitude shows that the development of the swinging motion induced by galloping is mainly driven by the yaw angle. As the oscillations are quasi-sinusoidal and $|\beta|$ reaches quite low values (below 15°), it is possible to simply link $|\beta|_{max}$ to the the maximal absolute angle ϕ reached

in each period of oscillation $|\phi|_{max}$ and U^* (eq. 12) where $|\dot{\phi}|_{max} \approx 2\pi f_0 |\phi|_{max}$.

$$|\beta|_{max} \approx tan(|\beta|_{max}) = \frac{L|\dot{\phi}|_{max}}{U_0} \approx \frac{2\pi f_0 L|\phi|_{max}}{U_0} = 2\pi \frac{L}{D} \frac{|\phi|_{max}}{U^*} \tag{12}$$

Knowing that L/D is constant in the experiments, the similitude in $|\beta|_{max}$ means that the higher the reduced velocity, the larger the amplitude of the pendulum oscillations. For U^* from 39.9 to 57, the experiments had to be stopped because the mechanical setup did not allow oscillations with $|\phi|_{max}$ larger than 50°. However, the beginning of saturation of the oscillations is visible for $U^* = 39.9$ but could not be observed entirely (figure 7a). Thus, according to the previous remark, lower reduced velocities down to 18.5 are investigated to observe the full development of the swinging motion, including the saturation phase that is expected to occur at lower amplitudes of oscillations in ϕ. No static measurements have been done at these lower reduced velocities.

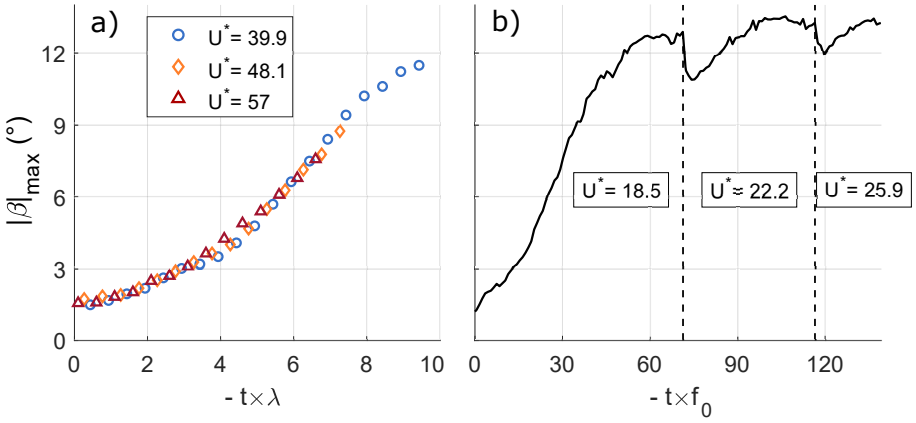

Figure 7: Evolution of the maximal absolute yaw angle reached in a period of oscillation $|\beta|_{max}$
a) for three different reduced velocities with the reduced time $t^* = -\lambda t$
b) for 3 successive low reduced velocities U^* to investigate the saturated state; the JV wind tunnel velocity U_0 is increased step by step in this dedicated experiment

Among the experiments realized at lower U^*, one consists of investigating the saturated state of the motion for three successive reduced velocities. The experiment starts from rest at $U^* = 18.5$. Once the swinging motion is saturated, U^* is increased up to 22.2 by increasing U_0. The process is then repeated to investigate $U^* = 25.9$. Figure 7b presents the evolution of the envelope of $|\beta|_{max}$ during this experiment and clearly shows a saturation of the motion for $|\beta|_{max} \approx 12 - 13°$ for the three reduced velocities investigated. One can notice a slight increase in the amplitude of saturation as U^* increases.

The fact that the motion saturates indicates a balance between the energy received by the pendulum from the flow and the energy given by the pendulum to the flow. An analysis of the energy transfers is thus realized to characterize the different phases of the swinging motion. The instantaneous power P received by the cube pendulum

from the flow (eq. 13) is derived from the cube velocity V and the aerodynamic loads F along $\vec{e_\phi}$, which is computed with the instantaneous pressure measurements. The energy W received during one period of oscillation is derived from P as detailed in eq. 14, and scaled by the mean kinetic energy of the flow crossing the cube section in one period of oscillation (eq. 16). P^* and W^* refer respectively to the reduced instantaneous power and the reduced periodic energy received by the cube pendulum. $P > 0$ when C_ϕ and β have opposite signs (eq. 13).

$$P = V \cdot F = L\dot{\phi} \times \tfrac{1}{2}\rho S U^2 C_\phi = -\tfrac{1}{2}\rho S U^3 \, C_\phi \, tan(\beta) \tag{13}$$

$$W = \int_t^{t+T_0} P \, dt = T_0 \, \langle P \rangle_{T_0} \tag{14}$$

$$P^* = \frac{P}{\frac{1}{2}\rho S U_0^3} = -\left(\frac{U}{U_0}\right)^3 C_\phi \, tan(\beta) \tag{15}$$

$$W^* = \frac{W}{\frac{1}{2}\rho S U_0^3 T_0} = \langle P^* \rangle_{T_0} \tag{16}$$

Figure 8 presents the energy transfers between the cube pendulum and the flow for $U^* = 18.5$ and $U^* = 39.9$. In the quasi-exponential part of the amplification, $P^* \geq 0$ so the pendulum is always accelerated by the flow. This quasi-exponential phase is similar for the two reduced velocities in terms of energy transfers. Around $|\beta|_{max} = 6 - 7^\circ$, the growth rate of the amplitude of oscillation starts decreasing and the saturation process starts, with a plateau followed by a decrease of W^* down to zero. For $U^* = 18.5$, an increasing power loss is observed during the transition part of the saturation phase. However, no power loss is observed for $U^* = 39.9$.

To quantify these periodic energy gains and losses, W_R and W_L are introduced respectively as the cumulative energy received by the pendulum and the cumulative energy lost by the pendulum over one period of oscillation. Both are positive values defined such as $W = W_R - W_L$. The evolution with $|\beta|_{max}$ of the periodic loss-gain ratio W_L/W_R is shown for various reduced velocities from 18.5 to 48.1 in figure 9. As previously observed in figure 8, the energy loss is non-negligible from $|\beta|_{max} \approx 6^\circ$ for the lowest reduced velocity $U^* = 18.5$. This is not the case for $U^* \geq 39.9$ for which $W_L/W_R \approx 0$: the power loss is negligible. Consequently, the mechanism of saturation depends on the reduced velocity.

The quasi-steady non-linear model briefly introduced in section 3.1 (eq. 3) is used to obtain the evolution of W_L/W_R under the quasi-steady assumption from the static aerodynamic coefficients displayed in figure 9. The static coefficients for $U^* = 18.5$ are missing in this study, but it is assumed that they are close to the static coefficients obtained at a higher Reynolds number of the same order of magnitude. In this range of Reynolds number ($O(10^5)$), static coefficients are expected to remain fairly constant for this cubic geometry with sharp edges. The hypothetical quasi-steady behavior at $U^* = 18.5$ is thus approached using the static coefficients obtained at a higher flow velocity.

The model predicts an energy loss from $|\beta|_{max} \approx 12^\circ$ and a saturation at a maximum yaw angle $|\beta|_{max} \approx 14.5^\circ$ for all U^*. This is consistent with the change of sign of $\overline{C_\phi}$ around the reattachment angle pointed out in section 4. However, this does not match with the case at $U^* = 18.5$ for which the loss-gain ratio starts a slow increase at $|\beta|_{max} \approx 6^\circ$ and strongly increases from $|\beta|_{max} \approx 10^\circ$, values lower than in the quasi-steady case. As a consequence, a lower $|\beta|_{max}$ is reached in the saturated state (around 12.5°). This is also visible in figure 7b where the oscillations saturate at $|\beta|_{max}$ lower than 14.5°. The measurements at higher reduced velocities are more in agreement with the quasi-steady assumption as the energy loss-gain ratio is very

small. Thus, for the lowest reduced velocity investigated $U^* = 18.5$, the quasi-steady theory does not hold anymore, and it appears that unsteady phenomena come into play in the saturation process.

The different phases of the swinging motion are now investigated in detail to identify the unsteady flow mechanisms at stake in the development of the galloping instability

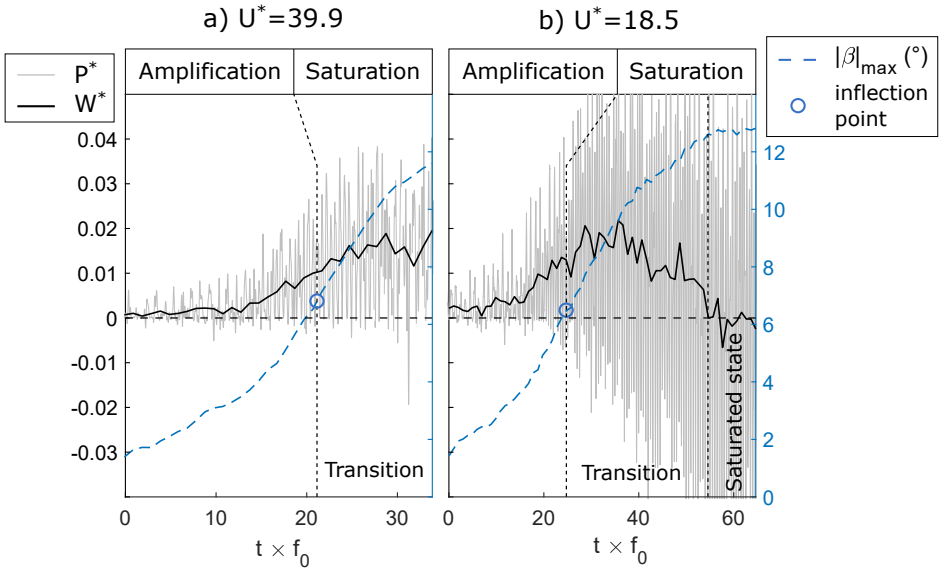

Figure 8: Energy transfers and time-evolution of $|\beta|_{max}$ during the swinging motion at $U^* = 18.5$ and $U^* = 39.9$, with the reduced instantaneous power P^* and the reduced periodic energy W^* received by the pendulum

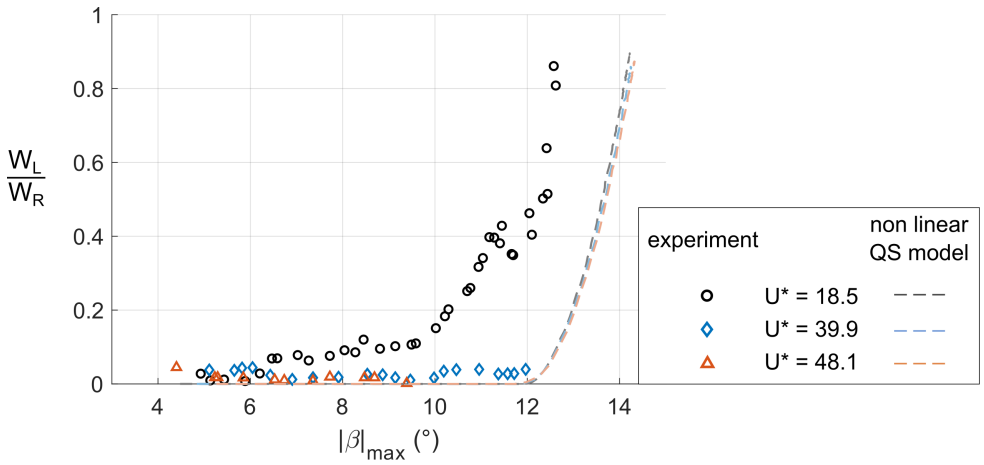

Figure 9: Periodic energy loss/gain ratio of the pendulum W_L/W_R for different reduced velocities according to the maximum absolute yaw angle reached in each period $|\beta|_{max}$;
Experimental measurements are compared with the results given by the non-linear quasi-steady model

5.2 The quasi-exponential amplification phase

The quasi-exponential amplification phase of the swinging motion is investigated from the pressure measurements to assess the quasi-steady hypothesis and tackle the mechanism of galloping instability. This phase corresponds approximately to $|\beta|_{max} \leq 6°$ for all the reduced velocities investigated. This is the value from which the growth rate of the amplitude of oscillation starts decreasing (figure 7 and 8). The local pressure measurements are spatially integrated to get the instantaneous aerodynamic loads acting on the cube during its swinging motion. Phase-averaging of these aerodynamic loads is performed to get the evolution of the dynamic loads with the yaw angle β. These dynamic loads are then compared to the mean static loads derived from pressure measurements on the static cube. In a typical setup involving a square cylinder with a spring-damper system, the quasi-steady theory is usually validated by comparing the oscillation amplitude of the experiment with the one predicted by the model [19]. The method used in this paper is more direct as the oscillation frequency is low and the dynamic loads are accessible and can be directly compared to the static ones.

The data of interest is phase-averaged in time over 3 periods of oscillations (approximately 1200 samples). The trials are repeated in the same configuration up to 3 times to increase the number of samples. The minimum number of samples used to get an average value is set to 48. From the standard deviation σ of the experimental coefficient C_ϕ obtained from static measurements at various yaw angles, a 95% confidence interval of the mean value can be derived as follows [31] : $I_{95\%} = \pm 1.96\sqrt{\sigma^2/N} \approx \pm 0.027$ (with $N = 48$ the minimum number of samples). This interval corresponds to $\pm 20\%$ of the absolute mean value of C_ϕ in static configuration at $\beta_0 = 6°$. It is acceptable in the scope of this study.

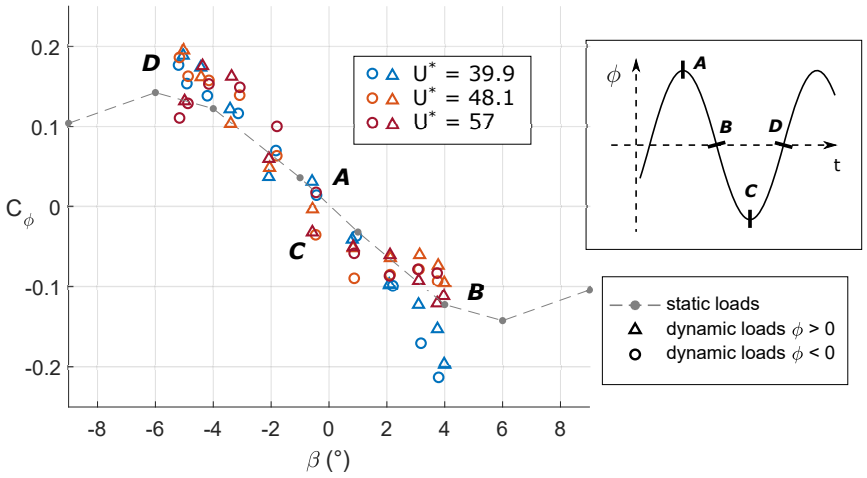

Figure 10: Evolution with β of the ynamic and static coefficient C_ϕ of the cube during the amplification phase, for several reduced velocities U^*

Figure 10 shows the evolution of the static and phase-averaged dynamic coefficients C_ϕ according to β, for several reduced velocities at $|\beta|_{max} \leq 5°$, so in the quasi-exponential amplification phase. The dynamic loads in the two half-periods of the swinging motion are collapse and fit well with the static loads. Thus, for each yaw angle investigated, the cube experiences the same force as if it was held stationary at the same yaw angle, which is the definition of a quasi-steady behavior. Consequently, the amplification phase is quasi-steady and the use of the quasi-steady theory is justified in the stability analysis. The negative slope of the aerodynamic force along $\vec{e_\phi}$ - characteristic of galloping - is observed on both static and dynamic loads evolutions. The quasi-linear evolution of C_ϕ around $\beta = 0$ also explains the quasi-exponential growth of the amplitude of oscillation like in a second order differential system, as obtained with the linearized momentum equation 8. Finally, C_ϕ and β have opposite signs as the slope is negative so the energy transfers are exclusively from the flow to the pendulum ($P \geq 0$ according to eq. 13), consistently with the energy transfers presented in figure 8.

As the quasi-steady theory is valid for low $|\beta|_{max}$, the mean static pressure distributions presented in figure 5 for the static yaw angle $\beta_0 = 1°$ and $\beta_0 = 4°$ can be used to understand the physical mechanisms driving the galloping instability. The local pressure distribution on the two sides of the cube is nearly uniform and the depression is larger on the windward side. This tends to amplify the motion as the resulting aerodynamic force aligns with the direction of motion. As discussed in section 4, these pressure patterns are related to non-symmetrical evolutions of the separated shear layers along the lateral faces and unbalanced flow velocity around the vertical leading edges of the cube. Nakamura [15] observed the same patterns from pressure measurements and flow visualization on a galloping square cylinder. Thus, the mechanism of galloping occurring on the cube pendulum and the one occurring on a bi-dimensional square cylinder seem to be the same despite the tridimensional shape of the cube.

5.3 The saturation phase

As in section 5.2, phase-averaging of the dynamic loads obtained from the pressure measurements is performed during the saturation phase of the motion. In a saturated state, more than 3 periods are used to process the phase-averaging. As explained in section 2.2, the uncertainty on the static yaw angle β_0 is responsible for the asymmetries in the cube pendulum dynamics visible in figure 11.

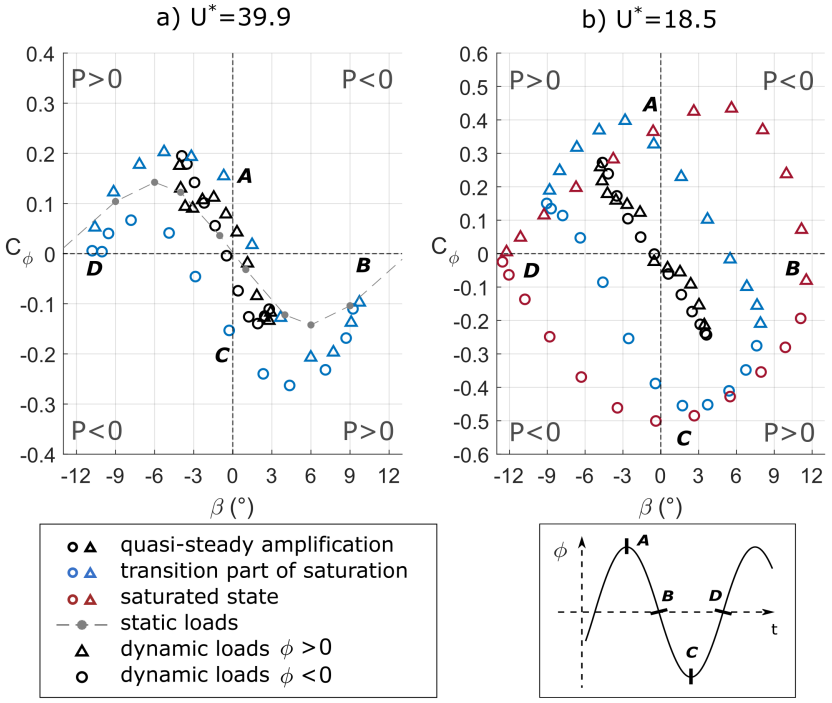

Figure 11: Evolution with β of the dynamic and static coefficient C_ϕ of the cube derived from the phase-averaged local pressure measurements during the saturation phase at $U^* = 39.9$ (a) and $U^* = 18.5$ (b);
The areas where the pendulum gains ($P > 0$) and loses ($P < 0$) power are separated by dotted lines

Initially superimposed at the end of the quasi-steady amplification phase, the dynamic loads of the two half-periods of oscillation ($\phi > 0$ and $\phi < 0$) dissociate to form a cycle during the saturation phase (figure 11). The cycle gets larger and larger until the saturated state is reached, which does not occur for $U^* = 39.9$ and higher reduced velocities as the experiments had to be stopped not to reach the mechanical limits of the setup in amplitude. In addition to the energy transfer analysis, these observations based on the dynamic loads confirm that unsteady phenomena occur during the saturation phase.

This unsteadiness produces an aerodynamic force opposed to the pendulum motion when the cube starts going down between A and B and between C and D in figure 11 : $\beta \cdot C_\phi$ - like $tan(\beta) \cdot C_\phi$ - becomes positive so P^* becomes negative (eq. 13).

The braking force increases as $|\beta|_{max}$ increases, and it balances the accelerating force in the saturated state for $U^* = 18.5$ (figure 8). Contrary to the case at $U^* = 18.5$, there is an aerodynamic braking force only at low $|\beta|$ for $U^* = 39.9$, so the power loss $P^* = C_\phi \, tan(\beta)$ remains low. This is consistent with the negligible resulting power loss observed for $U^* \geq 39.9$ in figure 9.

The aerodynamic behavior of the pendulum for $U^* = 39.9$ in figure 11a shows that, for the largest $|\beta|_{max}$ reached ($|\beta|_{max} \approx 9°$), the dynamic loads are nearly equals to the corresponding static loads. On the contrary, they are different for $\beta \approx 0$. This suggests that the dynamic loads drift from the static loads with a maximal difference around $\beta = 0$ (extreme positions of the pendulum) but both remain quite close to each other around the extreme yaw angles reached in a period of oscillation (vertical position). This is confirmed for $U^* = 39.9$ by the comparison between the distribution of the pressure coefficients C_p along the lateral faces of the cube for $|\beta|_{max} \approx 9°$ in figure 12.

The investigation of the time-evolution of β provides a better understanding of this phenomenon. As depicted in figure 13 for this sinusoidal motion, the time-variation rate of β, noted $|\dot{\beta}|$, is maximum in the vicinity of $\beta = 0$ while it reaches its minimum in the vicinity of $|\beta|_{max}$. Our interpretation is therefore that, at the maximum yaw angle $|\beta|_{max}$, the flow has more time to recover and to reorganize like in a quasi-steady configuration. The characteristic time of the variations of β can be defined as $T_\beta = |\beta|_{max}/|\dot{\beta}|_{\beta=0}$. As $|\dot{\beta}|_{\beta=0} \approx \omega_0 \, |\beta|_{max}$, T_β is basically $1/\omega_0$, or $T_0/2\pi$.

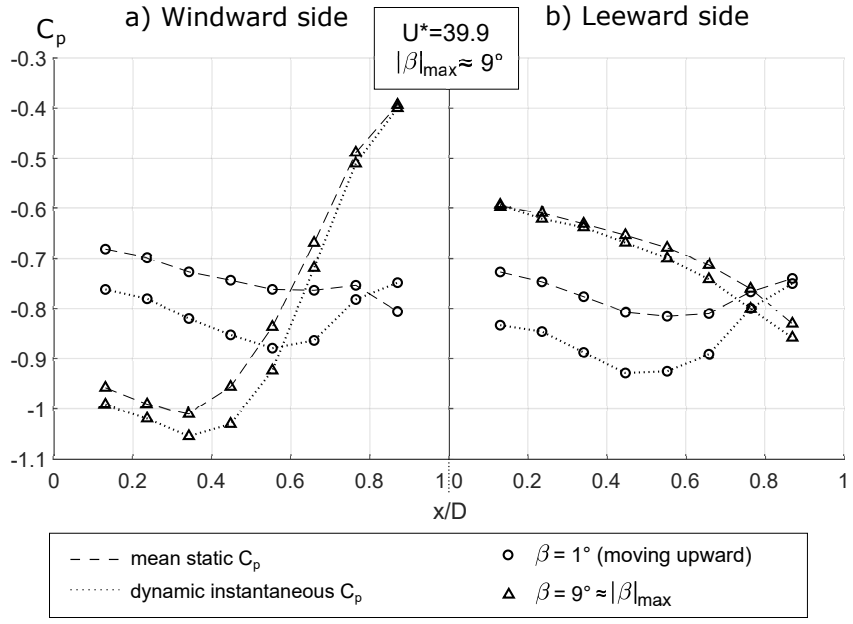

Figure 12: Comparison of the distribution of pressure coefficients C_p on the lateral faces of the cube for $|\beta|_{max} = 9°$ and $U^* = 39.9$, measured on the static cube and the swinging cube

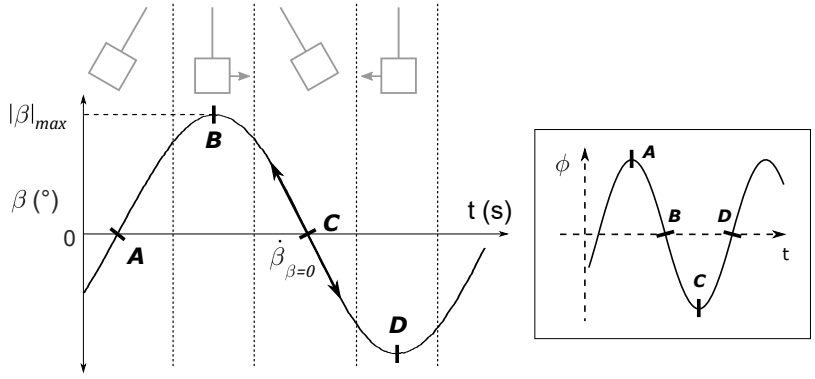

Figure 13: Time evolution of β during one period of oscillation

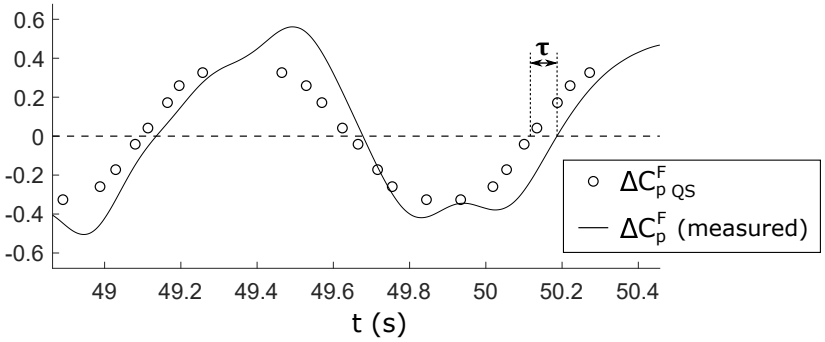

Figure 14: Phase shift between the measured ΔC_p^F and its value under the quasi-steady (QS) assumption $\Delta C_{p\ QS}^F$ during the saturation at $U^* = 39.9$; τ is the maximum time delay in half a period of oscillation

The ratio $T_\beta/T_{adv} = U^*/2\pi$ is of the order of 3 for $U^* = 18.5$, where $T_{adv} = D/U_0$ is the flow advective time. The pressure data can be used to study the response of the wake to the yaw angle variations imposed by the swinging motion. It is proposed here to make use of the two side frontmost probes A and B introduced in section 4, located on each side of the cube as depicted in figure 5, as a first indicator of the wake dynamics in response to a variation of β. The time evolution of the difference $\Delta C_p^F = C_p^A - C_p^B$ is investigated during the swinging motion. It can be compared to the quasi-steady evolution of the same quantity derived from static measurements for varying β, noted here $\Delta C_{p\ QS}^F$. As an example, figure 14 presents the comparison between ΔC_p^F and $\Delta C_{p\ QS}^F$ during the saturation phase for $U^* = 39.9$. A clear time delay is observed between the two quantities. In order to quantify this time delay, noting that $\Delta C_{p\ QS}^F = 0$ for $\beta = 0$, the time lag τ is defined for each half period of oscillation as $\tau = t(\Delta C_p^F = 0) - t(\Delta C_{p\ QS}^F = 0)$ – see figure 14 – which corresponds to the difference $\tau = t(\Delta C_p^F = 0) - t(\beta = 0)$.

The ratio $T_\beta/T_{adv} = U^*/2\pi$ compares the forcing time scale and the advective time scale. It is then interesting to compare the time lag τ with each of these time

scales. This is performed in figure 15 where τ is obtained using a sliding average over three periods of oscillations. In figure 15a, the quasi-steady dynamics observed for large U^* corresponds to $\tau \ll T_\beta$ whereas the departure from quasi-steady dynamics corresponds to $\tau \sim T_\beta$. τ also increases significantly with $|\beta|_{max}$ for $|\beta|_{max} \leq 6^\circ$ while a plateau of the ratio τ/T_β is reached for $|\beta|_{max} \geq 8^\circ$. Such behavior is believed to be associated with flow attachment along the windward surface for these large $|\beta|_{max}$, inducing a time lag driven by the slow transition between attached and detached states [32, 33] during the motion of the cube. This will be studied in a future experimental campaign using particle image velocimetry (PIV) measurements. Figure 15b presents the evolution of τ scaled by the flow advective time T_{adv}. With this scaling, a clear similitude is observed between all the reduced velocities which means that the flow response to the changes in upstream yaw angle drives the delay. For $|\beta|_{max} \geq 8^\circ$, $\tau/T_{adv} \sim 2$ whereas τ/T_{adv} is smaller in the fully separated regime.

Figure 16 provides a visualization of the phase averaged pressure distribution during half a period of oscillation in the saturated state for $U^* = 18.5$. The cube pendulum moves up between A and C and moves down between C and E. Flow reattachment is clearly observed in step A on the windward side around $|\beta| = |\beta|_{max}$. The braking effect observed for $U^* = 18.5$ when the pendulum goes downward (figure 11b) is found to be produced by suction on the leeward side visible in steps C and D of figure 16. The upstream part of the pressure distribution on the side faces is nearly identical in B and D despite a strongly opposite yaw angle (-8° and 8° respectively), indicating that the variation of β between B and D is too fast for the lateral separated regions to immediately reorganize. The resulting time lag between the pendulum and the wake dynamics appears while the pendulum moves up and persists while the cube moves down. It leads to a temporary suction on the leeward side and is thus responsible for the unsteady aerodynamic behavior.

Consistently, a higher reduced velocity produces a shorter time delay, which means a thinner cycle of dynamic loads (figure 11). The resulting braking force occurs at lower $|\beta|$ and produces a smaller energy loss: the pendulum dynamics gets closer to the quasi-steady dynamics.

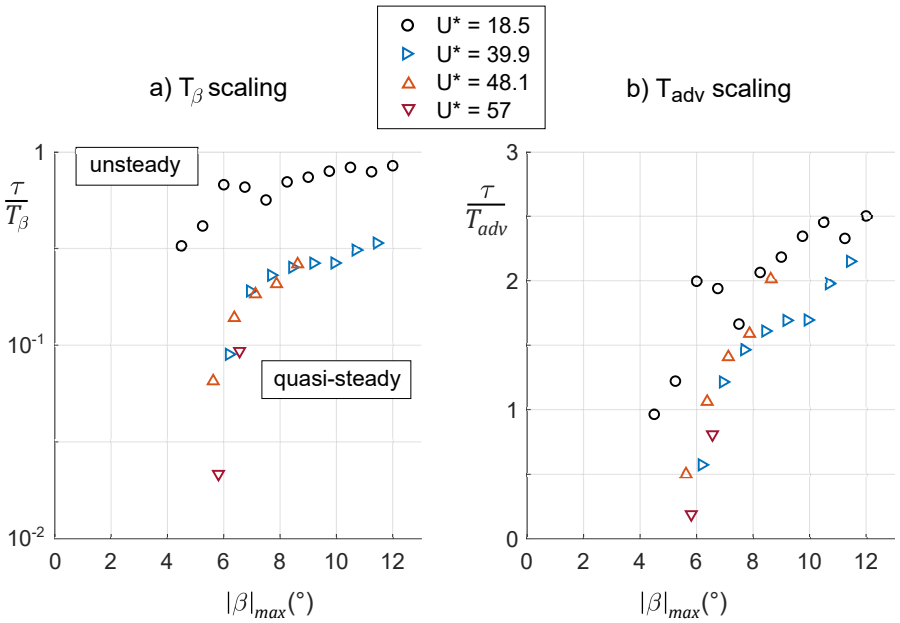

Figure 15: Evolution of the time delay τ with $|\beta|_{max}$
a) scaled by the β-variations time $T_\beta = T_0/2\pi$
b) scaled by the advective time $T_{adv} = D/U_0$

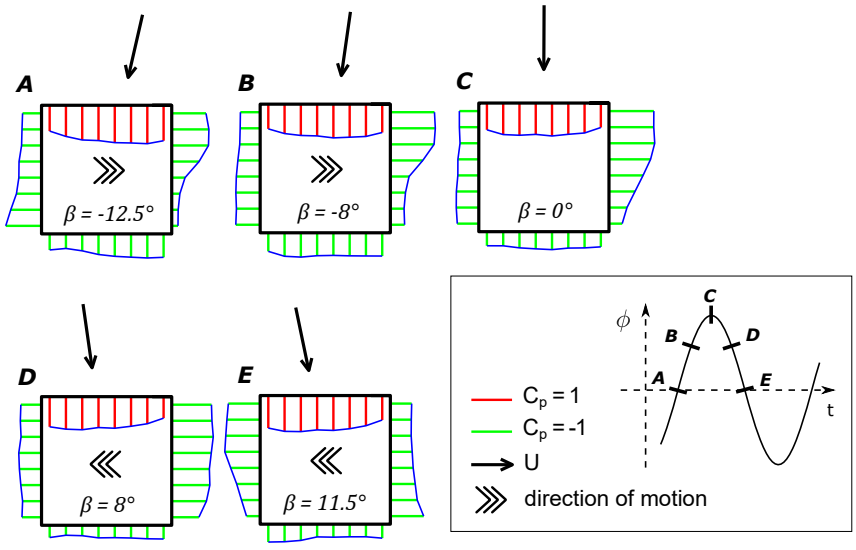

Figure 16: Distribution of phase-averaged pressure coefficient C_p at various yaw angles β during half a period of oscillation in saturated state for $U^* = 18.5$

6 Conclusions

A cube pendulum in a flow at high Reynolds number with low free-stream turbulence intensity exhibits a galloping instability on a wide range of reduced velocities. Galloping occurs when the cube makes a static yaw angle $\beta_0 \in [-9°, 9°]$ with the mean flow. A quasi-steady linear model based on the linearized momentum equations of the pendulum provides the same stability criterion as the Den Hartog criterion for bidimensional cylinders and proves to be a relevant tool for predicting the stability of the cube pendulum. Despite the tridimensional shape of the cube, the observed galloping instability is driven by the same physical mechanisms as the galloping instability observed on bidimensional square cylinders.

The pendulum swinging motion induced by galloping ends up saturated in amplitudes. Among the reduced velocities investigated, the lowest one - $U^* = 18.5$ - reveals unsteady phenomena during the saturation process. A phase delay between the wake and the pendulum dynamics produces an aerodynamic braking force when the cube pendulum moves down, which is responsible for a premature saturation of the pendulum oscillation. This aerodynamic time delay has been characterized and is found to scale with the flow advective time and to produce an unsteady effect only when it is of the order of magnitude of the maximum time-variation rate of the yaw angle β. This unsteady delay also seems to be influenced by separation-reattachment dynamics as a periodic reattachment occurs on the windward side of the cube. Consistently, for higher reduced velocities, the aerodynamic response delay is shorter and the cube pendulum follows a more quasi-steady behavior.

The study strongly relies on pressure measurements, however a velocity field is necessary to fully understand the cube pendulum wake dynamics, especially in unsteady configurations. A further study of the velocity field surrounding the cube could provide insight into the particular unsteady effects observed during saturation, allowing to investigate in detail the flow reorganization in the downward phase of the swinging motion. The investigation of low reduced velocities also turns out to be critical in future works about FSI on a bluff body pendulum. Indeed, for real-world applications concerning cable cars, for instance, the range of reduced velocities is low, and unsteady effects are expected to be dominant. Finally, more DoF, the shape of the bluff body, and the upstream flow turbulence are some factors whose influence on the pendulum dynamics is currently studied.

Acknowledgement

We are indebted to the French Agence Nationale pour la Recherche (ANR) through the ANR project Turb-Cab (ID ANR-22-CE22-0010) for financial support. The authors would like to warmly thank Mathieu Rossard for technical assistance.

Supplementary movie

A supplementary movie of the galloping cube pendulum observed in the Jules Verne wind tunnel for $\beta_0 = 0$ is available (galop_JV.mp4).

References

[1] I. Mehdipour et al. "Comprehensive experimental study on bluff body shapes for vortex-induced vibration piezoelectric energy harvesting mechanisms". In: *Energy Convers. Manag.: X* 13 (2022), p. 100174.

[2] G. V. Parkinson and N. P. H. Brooks. "On the aeroelastic instability of bluff cylinders". In: *J. Appl. Mech.* 28 (1961), pp. 252–258.

[3] J. P. Den Hartog. *Mechanical vibrations*. Courier Corporation, 1985.

[4] Y. Nakamura and Y. Tomonari. "Galloping of rectangular prisms in a smooth and in a turbulent flow". In: *J. Sound Vib.* 52.2 (1977), pp. 233–241.

[5] P. W. Bearman et al. "Experiments on flow-induced vibration of a square-section cylinder". In: *J. Fluids Struct.* 1.1 (1987), pp. 19–34.

[6] P. Hémon. *Vibrations des structures couplées avec le vent*. Editions Ecole Polytechnique, 2006.

[7] T. Oktay and C. Sultan. "Modeling and control of a helicopter slung-load system". In: *Aerosp Sci Technol* 29.1 (2013), pp. 206–222.

[8] L. Jin et al. "Exploring the impact of wind loads on tower crane operation". In: *Math. Probl. Eng.* 2020 (2020), pp. 1–11.

[9] J. Ye and J. Huang. "Analytical analysis and oscillation control of payload twisting dynamics in a tower crane carrying a slender payload". In: *MSSP* 158 (2021), p. 107763.

[10] K. Hofman. "Oscillation effects of ropeways caused by cross-wind and other influences". In: *Fme Trans.* 37.4 (2009), pp. 175–184.

[11] D. Bryja and M. Knawa. "Computational model of an inclined aerial ropeway and numerical method for analyzing nonlinear cable-car interaction". In: *Comput Struct* 89.21-22 (2011), pp. 1895–1905.

[12] J. M. W. Brownjohn. "Dynamics of an aerial cableway system". In: *Eng. Struct.* 20.9 (1998), pp. 826–836.

[13] R. D. Blevins. *Flow-induced vibration, 2nd edition*. Krieger Publishing Company, 2001.

[14] P. W. Bearman and E. D. Obasaju. "An experimental study of pressure fluctuations on fixed and oscillating square-section cylinders". In: *J. Fluid Mech* 119 (1982), pp. 297–321.

[15] Y. Nakamura, K. Hirata, and T. Urabe. "Galloping of rectangular cylinders in the presence of a splitter plate". In: *J. Fluids Struct.* 5.5 (1991), pp. 521–549.

[16] P. Han et al. "Nonlinear modeling of combined galloping and vortex-induced vibration of square sections under flow". In: *Nonlinear Dyn.* 103 (2021), pp. 3113–3125.

[17] G. V. Parkinson. "Wind-induced instability of structures". In: *Philos. trans., Math. phys. eng. sci.* 269.1199 (1971), pp. 395–413.

[18] J. D. Smith. "An experimental study of the aeroelastic instability of rectangular cylinders". PhD thesis. University of British Columbia, 1962.

[19] G. V. Parkinson and J.D. Smith. "The square prism as an aeroelastic non-linear oscillator". In: *Q. J. Mech. Appl. Math.* 17.2 (1964), pp. 225–239.

[20] H. Kozmar. "Flow, turbulence and surface pressure on a wall-mounted cube in turbulent boundary layers". In: *J. Wind Eng. Ind. Aerodyn.* 210 (2021), p. 104503.

[21] J. Zhao et al. "Flow-induced vibration of a cube orientated at different incidence angles". In: *J. Fluids Struct.* 91 (2019), p. 102701.

[22] R.N. Govardhan and C. H. K. Williamson. "Vortex-induced vibrations of a sphere". In: *J. Fluid Mech.* 531 (2005), pp. 11–47.

[23] P. Hémon and F. Santi. "On the aeroelastic behaviour of rectangular cylinders in cross-flow". In: *J. Fluids Struct.* 16.7 (2002), pp. 855–889.

[24] A. S. Ramamurthy and P. M. Lee. "Wall effects on flow past bluff bodies". In: *J. Sound Vib.* 31.4 (1973), pp. 443–451.

[25] J. B. Barlow, W. H. Rae, and A. Pope. *Low-speed wind tunnel testing.* John Wiley & sons, 1999.

[26] S. Sharma et al. "Wall effect on fluid–structure interactions of a tethered bluff body". In: *Phys. Lett. A* 377.34-36 (2013), pp. 2079–2082.

[27] G. S. West and C. J. Apelt. "The effects of tunnel blockage and aspect ratio on the mean flow past a circular cylinder with Reynolds numbers between 10^4 and 10^5". In: *J. Fluid Mech.* 114 (1982), pp. 361–377.

[28] T. Igarashi. "Characteristics of the flow around a square prism". In: *J. Jpn. Soc. Mech. Eng.* 27.231 (1984), pp. 1858–1865.

[29] J. M. Robertson et al. "Wall pressures of separation—reattachment flow on a square prism in uniform flow". In: *Journal of Wind Engineering and Industrial Aerodynamics* 2.4 (1978), pp. 345–359.

[30] N. J. Cherry, R. Hillier, and M. E. M. P. Latour. "Unsteady measurements in a separated and reattaching flow". In: *J. Fluid Mech* 144 (1984), pp. 13–46.

[31] L. H. Benedict and R. D. Gould. "Towards better uncertainty estimates for turbulence statistics". In: *Exp Fluids* 22.2 (1996), pp. 129–136.

[32] A. Darabi and I. Wygnanski. "Active management of naturally separated flow over a solid surface. Part 1. The forced reattachment process". In: *J. Fluid Mech.* 510 (2004), pp. 105–129.

[33] A. Darabi and I. Wygnanski. "Active management of naturally separated flow over a solid surface. Part 2. The separation process". In: *J. Fluid Mech.* 510 (2004), pp. 131–144.